ELSEVIER
Science Press
Available online at www.sciencedirect.com
ScienceDirect
Trans. Nonferrous Met. Soc. China 30(2020) 2681−2696
Transactions of Nonferrous Metals Society of China
www.tnmsc.cn

# $\alpha''$ phase-assisted nucleation to obtain ultrafine $\alpha$ precipitates for designing high-strength near-$\beta$ titanium alloys

Zhen-yu WANG[1,2], Li-bin LIU[1,2], Di WU[1,2,3], Li-gang ZHANG[2], Wan-lin WANG[3], Ke-chao ZHOU[1]

1. State Key Laboratory of Powder Metallurgy, Central South University, Changsha 410083, China;
2. School of Materials Science and Engineering, Central South University, Changsha 410083, China;
3. School of Metallurgy and Environment, Central South University, Changsha 410083, China

Received 25 April 2020; accepted 28 September 2020

**Abstract:** The diffusion-multiple method was used to determine the composition of Ti−6Al−4V−*x*Mo−*y*Zr alloy ($0.45<x<12$, $0.5<y<14$, wt.%), which can obtain an ultrafine $\alpha$ phase. Results show that Ti−6Al−4V−5Mo−7Zr alloy can obtain an ultrafine $\alpha$ phase by using the $\alpha''$ phase assisted nucleation. The bimodal microstructure obtained with the heat-treatment process can confer the alloy with a good balance between the strength and plasticity. The deformation mechanism is the dislocation slip and the $\{1\bar{1}01\}$ twinning in the primary $\alpha$ phase. The strengthening mechanism is $\alpha/\beta$ interface strengthening. The interface of $(0001)_\alpha/(110)_\beta$ has a platform−step structure, whereas $(\bar{1}\bar{1}20)_\alpha/(\bar{1}11)_\beta$ interface is flat with no steps.

**Key words:** alloy design; high-strength titanium alloy; $\alpha''$ phase; $\alpha/\beta$ interface; twin deformation

## 1 Introduction

Titanium alloys are used in aerospace fields due to their high strength, high toughness, low density, high-temperature resistance, and corrosion resistance [1,2]. Recently, near $\beta$-type titanium alloys have become an important development trend of ultra-high-strength (strength exceeding 1250 MPa) titanium alloys [3]. The main reason for the high strength of $\beta$-titanium alloys is the fine secondary acicular $\alpha$ phase precipitated in the $\beta$ matrix [4]. These dispersed $\alpha$ phases and $\beta$ matrix form a large number of $\alpha/\beta$ phase boundaries, hindering dislocation slip and increasing the strength. Previous studies have involved the following factors affecting the precipitation of ultrafine $\alpha$ phase in the $\beta$ phase: (1) pseudo-spinodal mechanism involving composition fluctuations and (2) $\omega$-phase heterogeneous auxiliary nucleation mechanism involving structures [5,6]. References [7,8] showed that the use of the pseudo-spinodal mechanism in titanium alloys can obtain fine $\alpha$ phases. When the alloy composition is located near the intersection of the free energy curves of the $\alpha$ and $\beta$ phases, the free energy fluctuations with the fluctuation of the composition induce the precipitation of the fine $\alpha$ phase. NAG et al [9] observed in experiments that the $\alpha$ phase nucleated at the $\omega/\beta$ interface, and the $\omega$ phase was able to assist the $\alpha$ phase nucleation in obtaining fine $\alpha$ phases.

In recent years, another metastable $\alpha''$ phase in titanium alloys is attracting increased research interest. The $\alpha''$ phase is a combination of martensitic and orthorhombic structures, having a needle-like morphology [10]. In addition, the $\alpha''$ phase has lower strength and larger plasticity than

---

**Foundation item:** Projects (2016YFB0701301, 2018YFB0704100) supported by the National Key Technologies R&D Program of China; Projects (51901251, 51671218, 51501229) supported by the National Natural Science Foundation of China; Project (2020JJ5750) supported by the Natural Science Foundation of Hunan Province, China

**Corresponding author:** Di WU; Tel: +86-15084787759; Fax: +86-731-88876692; E-mail: wudi30@csu.edu.cn

DOI: 10.1016/S1003-6326(20)65412-7

the $\omega$ phase [11,12]. Thus, the $\alpha''$ phase produced by quenching can provide a potentially heterogeneous structure for the nucleation of $\alpha$ phase. However, current research on the $\alpha''$ phase is focused on the use of stress-induced $\alpha''$ martensitic transformation in reducing the elastic modulus of the alloy to design low-modulus biomedical titanium alloys [13,14]. At present, little research on the use of $\alpha''$ phase-assisted $\alpha$ phase nucleation to obtain ultrafine $\alpha$ phase has been found. Moreover, the mechanism of the influence of $\alpha''$ on the morphology of the $\alpha$ phase is still unclear. Therefore, the use of softer $\alpha''$ phase (than $\omega$ phase) assisted nucleation in obtaining the ultrafine $\alpha$ phase is a worthwhile idea in designing high-strength titanium alloys.

However, the composition of the alloy capable of obtaining the ultrafine $\alpha''$ phase is in a narrow composition range (approximately 2%), and many alloying elements are used in titanium alloy [15]. If the traditional trial and error method is performed to identify the critical stable composition, then the number of experiments would be huge, and a narrow optimal alloy composition would be difficult to find. However, the development of high-throughput diffusion-multiple technique has enabled the rapid exploration of the physicochemical properties of numerous alloy compositions [16]. ZHANG et al [17] used such a method to study the variations in hardness and elastic modulus of the Ti−Al−Nb system. COURY et al [18] studied the solid-solution strengthening effect of Co−Ni−Fe−Mn−Cr high-entropy alloy and successfully predicted the yield strength of different alloys. Therefore, the diffusion-multiple method can be an effective experimental method in quickly identifying and designing the optimal alloy composition.

This study aims to design ultra-high-strength titanium alloys using $\alpha''$ phase auxiliary nucleation, which produces an ultrafine $\alpha$ phase. Importantly, by systematically changing the heat-treatment condition, the microstructure is adjusted to achieve a good match between strength and plasticity. High-resolution transmission electron microscopy (HRTEM) is used to characterize the structure of the $\alpha/\beta$ interface and the deformation mechanism of the $\alpha$ phase, and subsequently the deformation and strengthening mechanisms are discussed.

## 2 Experimental

The diffusion multiple [19,20] is a group of alloys capable of interfacial contact in their design geometry to include several diffusion couples and triples in one sample. After long-time high-temperature annealing, the compositional gradient of the diffusion multiple was formed by interdiffusion. In the present research, the diffusion-multiple method was used to study the influence of the Zr and Mo contents on the microscopic structure and mechanical properties of Ti−6Al−4V (hereinafter referred to as Ti-64) alloy and design a new high-strength titanium alloy. The Ti-64−20Mo−20Fe−20Cr−45Zr diffusion multiple was produced (Fig. 1; notably, this work deals only with the Ti-64−20Mo−45Zr ternary system in the red box area of Figs. 1(a, b)). The elements of Mo and Zr used in this experiment had 99.9 wt.% in purity. The chemical composition (wt.%) of Ti-64 used to prepare the diffusion multiple in this experiment was 3.91 V, 6.37 Al, 0.13 Fe, 0.18 O, 0.02 C, 0.02 N, and the balanced Ti. The alloys of Ti-64−20Mo, Ti-64−20Fe, Ti-64−20Cr and Ti-64−45Zr were manufactured by arc melting under argon protection, and the arc melting was repeated four times to guarantee the homogeneity. The alloys were cut by electrical-discharge machining. The diffusion multiple included one Ti-64 brick of 10 mm × 10 mm × 10 mm, one Ti-64−20Fe and one Ti-64−20Mo plate of 10 mm × 10 mm × 2 mm, and one Ti-64−45Zr and one Ti-64−20Cr plate of 12 mm × 10 mm × 2 mm. The bonding faces of each block were ground and polished with 0.5 μm alumina slurry. The diffusion multiple was welded at 1000 °C for 4 h in a vacuum furnace ($\sim 1\times10^{-3}$ Pa). Moreover, the welded diffusion multiple was sealed in a vacuum quartz tube and annealed at 1100 °C for 240 h to form a composition gradient. Next, the diffusion multiples were solution-treated at 1050 °C for 6 h and quenched in water. Then, they were aged at 600 °C for 6 h, and cooled in air. The diffusion multiple was sectioned by electrical discharge machining, mounted, ground and polished using traditional metallo-graphic sample production techniques. Microhardness indentations were made at 1400 μm × 1400 μm (red box area in Fig. 1(a)) with the BUEHLER−5104 test system with an

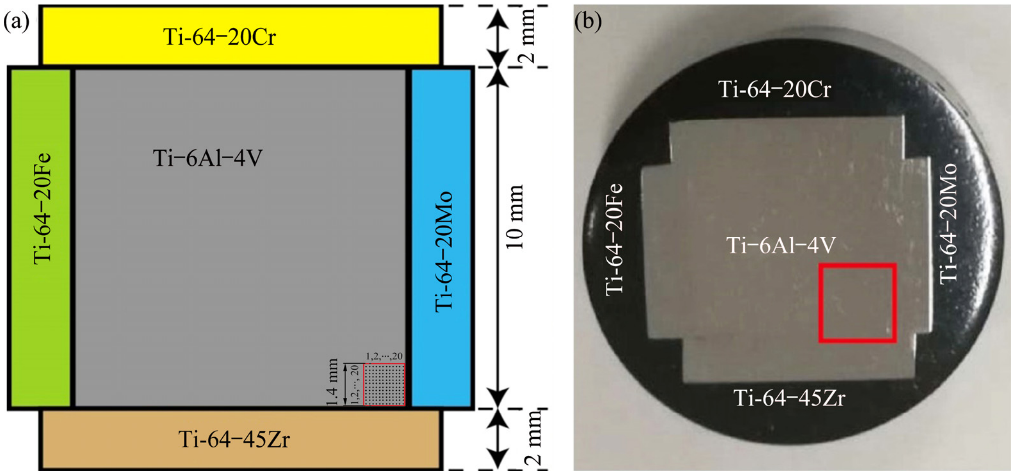

**Fig. 1** Ti-64−20Mo−45Zr−20Fe−20Cr diffusion-multiple model (red box area is studied area) (a) and photo (diffusion annealing at 1100 °C for 240 h) (b)

indentation load of 500 mN and dwell time of 15 s, and the composition and microstructure were characterized at 1−3 μm near the indentation. The composition analysis was performed on a JEOL JXA−8230 electron probe system at an acceleration voltage of 15 kV. Morphologies were characterized by NOVATM Nano SEM 230 field-emission SEM with a voltage of 25 kV and a distance of 5.5 mm.

Alloys with compositions of Ti-64−5Mo−7Zr (Ti-64-57) were double melted by vacuum arc remelting. The ingot was forged at $\beta$ single-phase into a square rod with size of 1000 mm × 80 mm × 40 mm. Then, the square rod was cut into blocks with size of 80 mm × 40 mm × 10 mm and was forged for the second time at around 840 °C ($\alpha/\beta$ phase region) to a square rod with size of 320 mm × 10 mm × 10 mm. The forged Ti-64-57 alloy was solution-treated at 800 and 900 °C for 0.5 h, air-cooled, and subjected to aging treatment at 500 and 600 °C for 6 h. Tensile tests were conducted on the samples by using an MTS 810 tensile-test system. HRTEM was performed on a Tecnai−G2−F20 system. The tensile specimen is bone-like with uniformly deformed part of 25 mm × 4 mm × 3 mm and the tensile strain rate was 2 mm/min. TEM was performed on a Titan G2 60−300 instrument with a working voltage of 300 kV. The fracture cross-section and fracture surface of the tensile specimens were observed using a TESCAN MIRA3 LMH scanning electron microscope with an acceleration voltage of 15 kV and a working distance of 15 mm.

## 3 Results

### 3.1 Composition and hardness distribution of Ti−6Al−4V−$x$Mo−$y$Zr (Ti-64-$xy$) alloys

The effects of Mo and Zr content changes on the microstructure and mechanical properties of Ti-64 alloy were studied by preparing a diffusion multiple with Ti-64 alloy as the matrix (Fig. 1). Furthermore, the composition distribution of the alloy (red box of Fig. 1; 1400 μm × 1400 μm) is determined by electron probe microanalysis (Fig. 2). The Mo and Zr elements diffuse from the right side (along the $x$-axis) and the lower side (along the $y$-axis) into the Ti-64 alloy to form a smooth composition gradient. Moreover, Ti−6Al−4V−$x$Mo−$y$Zr alloys (hereinafter referred to as Ti-64−$xy$) are obtained. The Mo content ranges from 0.35 to 12 wt.%, whereas the Zr content ranges from 0.5 to 14 wt.%. Zr achieves a longer diffusion distance and smoother diffusion curve than Mo because Mo diffuses more slowly than Zr [21].

The hardness distribution of the alloy (having a continuous composition gradient) is shown in Fig. 3 (the same region in Fig. 1) and Table 1. Along the $x$-axis, the Mo content of the base alloy Ti-64 is increased from 0 to 12 wt.% (Positions (a), (b), (c) and (d) in Fig. 3), and the hardness initially increases remarkably and then decreases. With 5−6 wt.% Mo, the alloy obtains higher hardness within a distinct band-like region. In the negative direction of the $y$-axis, the Zr content is increased

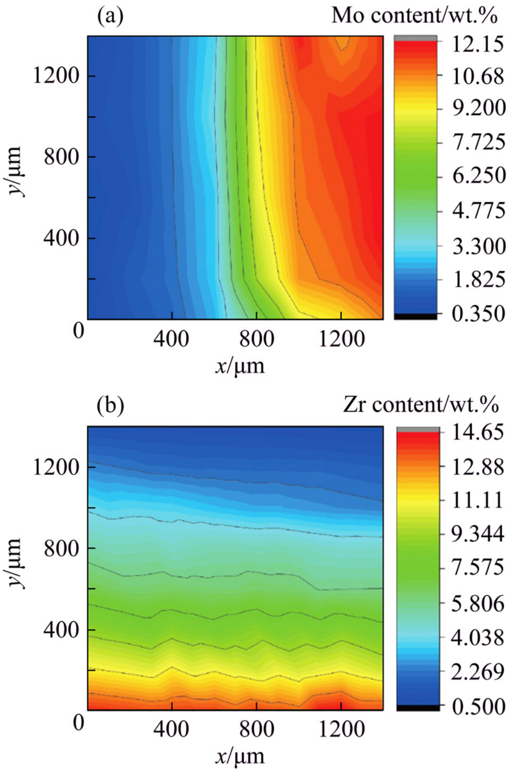

**Fig. 2** Distribution of Mo (a) and Zr (b) composition in red box area in Fig. 1

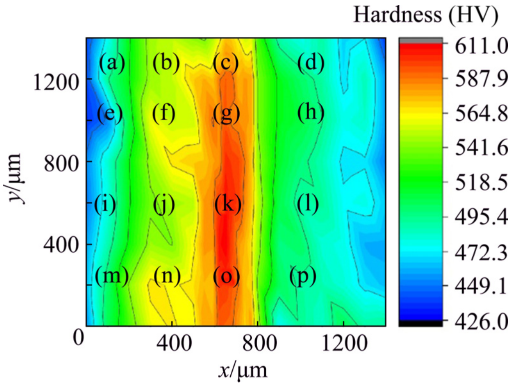

**Fig. 3** Hardness distribution in red box area in Fig. 1 (1100 °C quenching + 600 °C, 6 h aging)

from 1 to 14 wt.% (Positions (a), (e), (i) and (m) in Fig. 3), but the hardness keeps almost stable. In the high hardness region with 5 wt.% Mo, the hardness initially increases and then decreases with increasing Zr content. With 7 wt.% Zr, Ti-64-57 alloy obtains the highest hardness. The change in alloy hardness is closely related to the microstructure of the corresponding alloy.

**Table 1** Measured alloy composition, approximate nominal composition and hardness

| Measured composition/wt.% | | | | Approximate nominal composition/wt.% | Hardness (HV) |
|---|---|---|---|---|---|
| Mo | Zr | Al | V | | |
| 1.41 | 0.95 | 6.04 | 3.81 | Ti−6Al−4V−1Mo−1Zr | 459 |
| 3.13 | 1.17 | 5.93 | 3.96 | Ti−6Al−4V−3Mo−1Zr | 526 |
| 5.44 | 1.24 | 6.26 | 4.29 | Ti−6Al−4V−5Mo−1Zr | 593 |
| 8.82 | 1.59 | 6.30 | 4.01 | Ti−6Al−4V−9Mo−1Zr | 505 |
| 1.36 | 3.17 | 6.19 | 3.91 | Ti−6Al−4V−1Mo−3Zr | 462 |
| 3.07 | 3.23 | 6.89 | 4.30 | Ti−6Al−4V−3Mo−3Zr | 547 |
| 5.28 | 3.24 | 6.58 | 4.17 | Ti−6Al−4V−5Mo−3Zr | 601 |
| 8.85 | 3.37 | 6.44 | 3.96 | Ti−6Al−4V−9Mo−3Zr | 521 |
| 1.33 | 6.96 | 6.08 | 3.91 | Ti−6Al−4V−1Mo−7Zr | 479 |
| 3.27 | 6.72 | 6.28 | 4.18 | Ti−6Al−4V−3Mo−7Zr | 546 |
| 5.19 | 6.92 | 6.37 | 3.79 | Ti−6Al−4V−5Mo−7Zr | 611 |
| 8.34 | 7.13 | 6.06 | 3.93 | Ti−6Al−4V−9Mo−7Zr | 518 |
| 1.27 | 8.51 | 6.16 | 4.00 | Ti−6Al−4V−1Mo−9Zr | 484 |
| 2.98 | 8.88 | 6.30 | 4.39 | Ti−6Al−4V−3Mo−9Zr | 552 |
| 5.08 | 9.06 | 6.47 | 4.01 | Ti−6Al−4V−5Mo−9Zr | 594 |
| 8.63 | 9.24 | 6.22 | 4.32 | Ti−6Al−4V−9Mo−9Zr | 516 |

### 3.2 Microstructure evolution of Ti-64-*xy* alloy

Figure 4 shows microstructures of the alloy (with different compositions) at each position in Fig. 3. With increasing Mo content, the thickness of the $\alpha$ lath in the alloy gradually becomes less. At approximately 5 wt.% Mo, the alloy obtains a fine $\alpha$ lath (Figs. 4(c, g, k, o)), and then the $\alpha$ lath gradually coarsens with increasing Mo content. The effect of the change in Zr content on the $\alpha$ phase morphology of the alloy is similar to that on the hardness. At low Mo content, the $\alpha$ lath gradually becomes thinner with increasing Zr content. Conversely, at approximately 5 wt.% Mo, the $\alpha$ lath initially becomes thin and then wide with increasing Zr content (Figs. 4(c, g, k, o)). However, at approximately 9 wt.% Mo, the thickness of the $\alpha$ lath increases with increasing Zr content (Figs. 4(d, h, l, p)). Regarding the alloy hardness, the alloy composition of Ti-64-57 reaches its maximum value with the finest $\alpha$ phase structure. Similar to the previous research results [22], the thickness of the $\alpha$ lath directly affects alloy hardness. Given that the fine $\alpha$ phase produces more $\alpha/\beta$ interfaces, the slip that effectively blocks dislocations increases the alloy hardness. Furthermore, due to the differences in atomic radii of Mo, Zr and Ti, the solution-strengthening effect of Mo and Zr [23,24] on Ti-64-57 alloy requires consideration even if it seems weaker than microstructural strengthening.

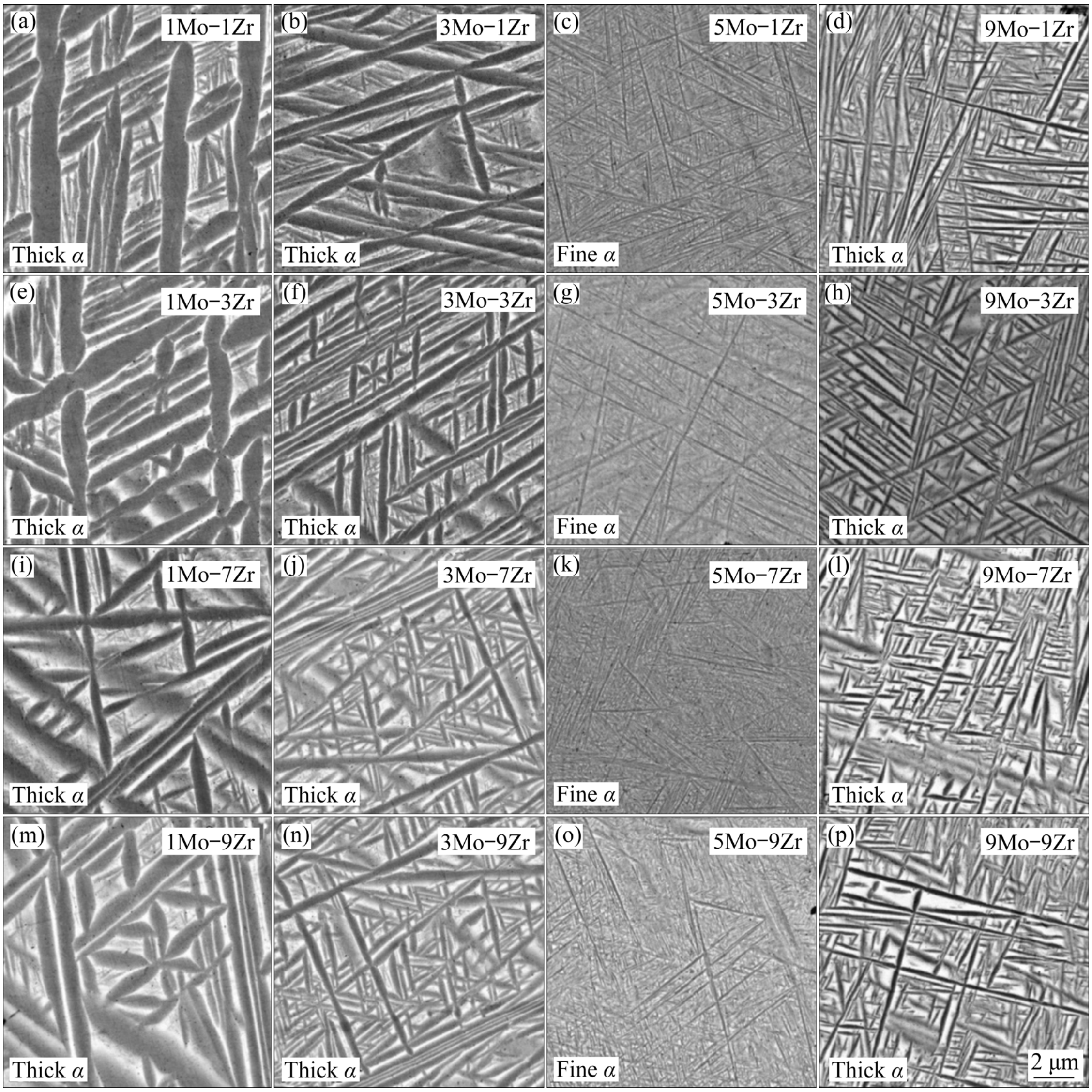

**Fig. 4** SEM images of Ti-64-*xy* alloys at different positions in Fig. 3 (1050 °C quenching + 600 °C, 6 h aging)

The microstructure changes of the alloy in the solution-quenching state (before aging) (Fig. 5) are studied to determine the morphology evolution of the $\alpha$ phase in Ti-64-*xy* alloys with the composition changes. The matrix Ti-64 alloy undergoes a $\beta\rightarrow\alpha'$ martensitic transformation during quenching due to the solution treatment of the alloy in the $\beta$ phase region. With increasing Mo content (Figs. 5(a, b, c, d)), the martensitic sheets become thin. Furthermore, a fine martensite structure is observed at 5 wt.% Mo, whereas the alloy obtains a single $\beta$ structure at ≥7 wt.% Mo, (Figs. 5(d, h, l, p)). The addition of Zr has few effects on the thickness of $\alpha$ martensite in the alloy, and the thickness of the $\alpha$ phase in the alloy decreases with increasing Zr content. At 5 wt.% Mo and ≥7 wt.% Zr, the alloy produces a single $\beta$ phase (Fig. 5(k)).

In general, with increasing Zr and Mo contents, the $\alpha'$ martensite lath initially becomes thin, and then a single $\beta$ phase is obtained. Considering that Mo is a strong $\beta$-stabilizing element and Zr is a weak $\beta$-stabilizing element (also known as a neutral element), the addition of Zr and Mo is bound to increase the stability of the $\beta$ phase and inhibit the $\beta\rightarrow\alpha'$ transition. During quenching, the starting and finishing temperatures of the martensite transition decrease and the growth (roughening) time shortens. Consequently, the thickness of the $\alpha'$ lath decreases. With further increasing Mo and Zr content, the $\beta\rightarrow\alpha'$ transition is completely suppressed. In addition, the starting temperature of the martensite transition is lowered below room temperature, and the alloy obtains a single $\beta$ structure. By comparing Fig. 5

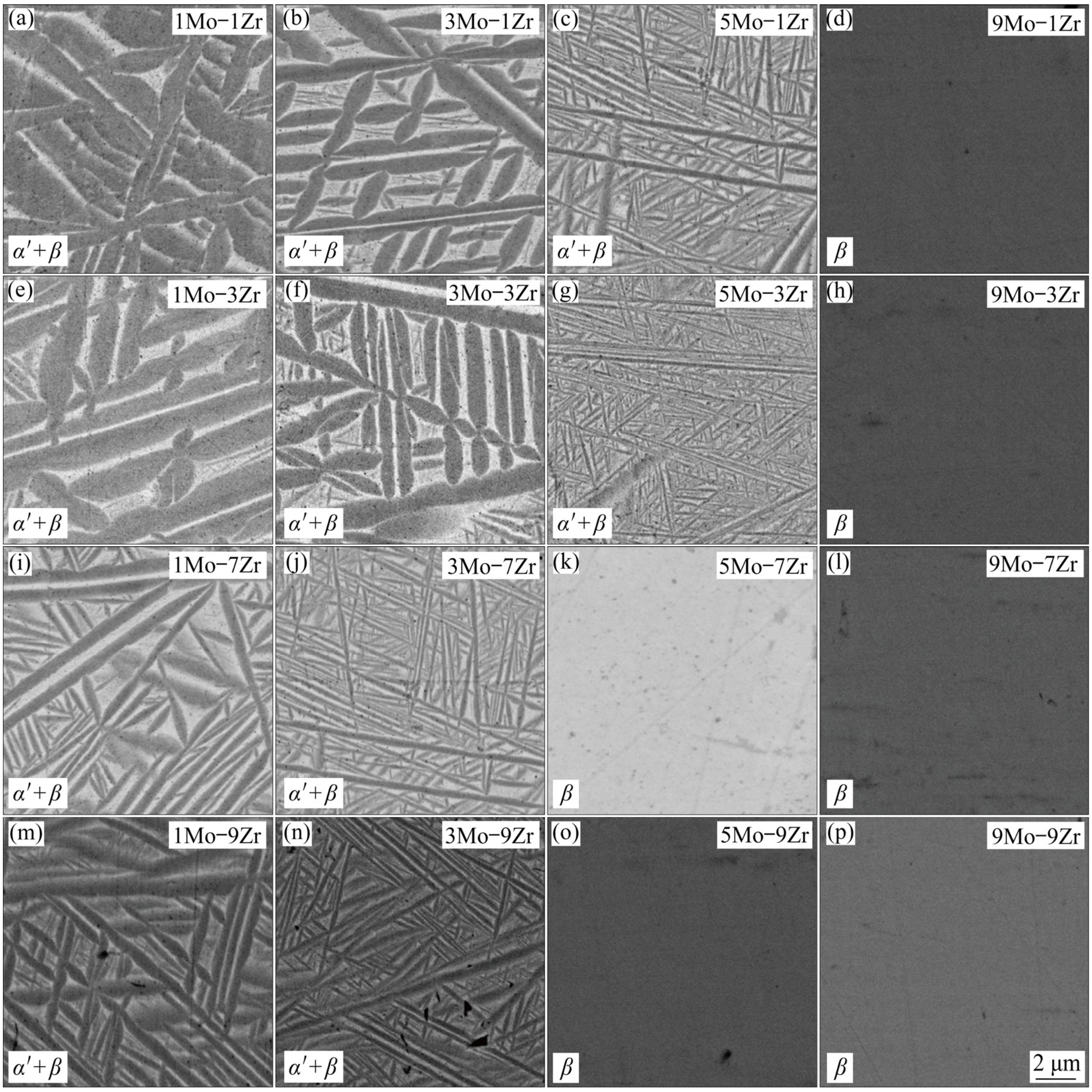

**Fig. 5** SEM microstructures of Ti-64-*xy* alloys at different positions in Fig. 3 (1050 °C quenching)

with Fig. 4, the thickness of the α phase during aging depends on the thickness of the α′ martensite when the alloy undergoes martensite transformation during quenching. When a single β phase is obtained during quenching, the thickness of the α phase during aging depends on the stability of the β phase. Moreover, at low Mo and Zr contents, the stability of β phase is low and the β→α transition has a larger driving force, resulting in a high nucleation rate that produces a fine α structure (Fig. 4(k), Ti-64-57). Furthermore, with increasing Zr and Mo contents, the stability of β phase increases and the driving force and nucleation rate of the β→α transition are lowered, resulting in increased thickness of the α phase (Fig. 4(p), Ti-64-99).

### 3.3 Transmission electron microscopy (TEM) analysis of Ti-64-57 alloy

A detailed TEM characterization of the Ti-64-57 alloy is performed in the quenched and aged states (Fig. 6) to explore how Ti-64-57 alloy obtained the finest α phase in the Ti-64-*xy* system. The TEM bright-field image shows that the alloy is not composed of a single β phase in the quenched state. In addition, a nanometer-sized acicular precipitate that has two variants arranged at 60° is observed in the β matrix (Fig. 6(a)). The dark-field image shows a precipitate phase with a length of approximately 100 nm and a thickness of 10 nm (Fig. 6(b)), and diffraction spots identify these precipitates as the α″ phase (Fig. 6(c)). Such results indicate that the alloy undergoes β→α″ transition

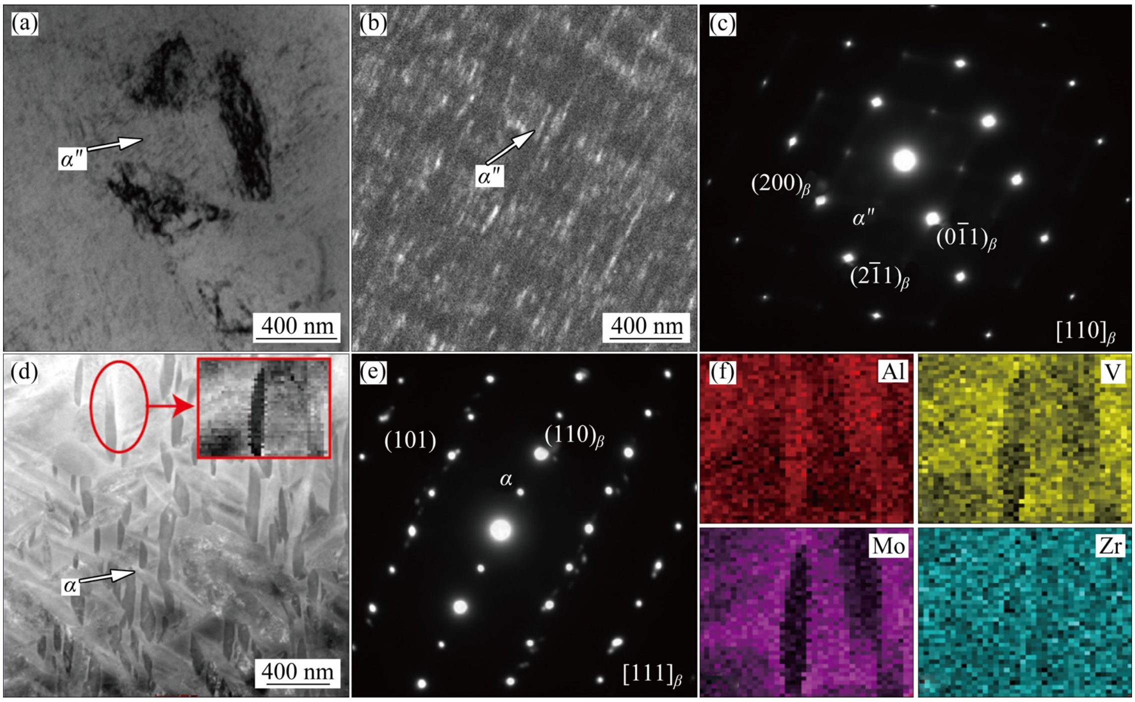

**Fig. 6** TEM images of Ti-64-57 alloy quenched at 1050 °C (a−c) and aged at 600 °C (d−f): (a) Bright-field image of $\alpha''$ phase with two variants; (b) Dark-field image of $\alpha''$ phase; (c) Selected electron diffraction in $[110]_\beta$ direction; (d) $\alpha$ phase with variants; (e) Selected electron diffraction in $[111]_\beta$ direction; (f) Distribution of elements in red box area in Fig. 6(d)

during quenching and that the $\alpha''$ phase may affect the morphology of the $\alpha$ phase during aging. The TEM morphologies (Figs. 6(d, e)) of the alloy show that three variants of the $\alpha$ phase are crossed by 60° and distributed in the $\beta$ phase. The length of the $\alpha$ phase is approximately 500 nm, and the thickness is 100 nm. A qualitative analysis of the composition of the $\alpha$ and $\beta$ phases shows that Al element is concentrated in the $\alpha$ phase, Mo and V elements are concentrated in the $\beta$ phase, and Zr element has a large solubility in $\alpha$ and $\beta$ phases.

The $\alpha''$ phase is an orthorhombic martensite generally considered as a transitional state of $\beta\rightarrow\alpha'$ transition [12]. Generally, the microscopic structure of $\alpha''$ is fine and needle-like, whereas that of $\alpha'$ is coarse and lath-shaped [11]. Previous studies [25] have shown that the $\alpha''$ phase affects the morphology of the $\alpha$ phase during aging, i.e., the transformation $\alpha''\rightarrow\alpha''_{\text{Mo-rich}}+\alpha''_{\text{Mo-lean}}\rightarrow\alpha+\beta$ is bound to occur. Moreover, considering that the quenched alloy has an ultrafine $\alpha''$ structure before aging, $\alpha''$ and $\alpha$ phases have variants crossed at 60°. As a result, the quenched $\alpha''$ phase may provide a heterogeneous nucleation sites for the $\alpha$ phase in the aging stage, thereby assisting the nucleation and improving the nucleation efficiency of the $\alpha$ phase. In general, the composition of Ti-64-57 alloy is in the critical components of $\beta\rightarrow\alpha'$ transition. Moreover, Ti-64-57 alloy has the lowest $\beta$ stability resulting in the largest $\alpha$ phase nucleation driving force in the aging stage. The presence of the $\alpha''$ phase reduces the nucleation work of the $\alpha$ phase [26], and the combination of the two factors gives the alloy the finest $\alpha$ structure.

It should be pointed out that there is no direct experimental evidence that $\alpha''$ phase assists $\alpha$ phase nucleation. The $\alpha''$ phase may be dissolved during aging process. The research of ZHENG et al [27] showed that through a two-stage aging treatment, the $\omega$ phase could play an indirect role in the nucleation of the $\alpha$ phase. The high-temperature aging dissolves the isothermal $\omega$ phase, and the lattice distortion and composition fluctuation of the $\beta$ matrix caused by the $\omega$ phase affect the nucleation of the $\alpha$ phase. The research of XIAO et al [28] obtained similar results. It is undeniable that quenching the $\alpha''$ phase will inevitably cause lattice distortion, and it is very likely that the alloy composition has also been partitioned during the quenching [22,29]. Previous studies have shown that the influence of $\omega$ to $\alpha$ phase nucleation seems to be difficult to eliminate. Therefore, we conclude that $\alpha''$ may provide a heterogeneous nucleation sites for the $\alpha$ phase during aging.

### 3.4 Microstructure and mechanical properties of forged Ti-64-57 alloy

A large piece of Ti-64-57 is cast and forged. The alloy undergoes aging treatment after solid solution treatment in the $\beta$ phase region (900 °C) and the $\alpha+\beta$ phase region (800 °C). The alloy is then subjected to microstructure observation and tensile tests. The SEM microstructures of the alloy are shown in Fig. 7. The alloy that is solution-treated in the $\beta$ region and aged has acicular $\alpha$ phase. When the aging temperature is 600 °C, the $\alpha$ phase is coarser, and when the aging temperature is 500 °C, the $\alpha$ phase becomes thinner. There is primary $\alpha$ phase in the alloy after solution treatment in the $\alpha+\beta$ region. The thickness of the primary $\alpha$ phase of the alloy is about 1 μm, and the length is 2−3 μm. The volume fraction of the primary $\alpha$ phase is about 26.7%. At the same aging temperature, the size (especially the length) of the acicular $\alpha$ phase after solid solution in the $\alpha+\beta$ phase region is significantly smaller than that in the $\beta$ region. There are two reasons for this: (1) The existence of primary $\alpha$ phase hinders the growth of secondary $\alpha$ phase; (2) Primary $\alpha$ causes changes in the composition of the $\beta$ matrix and affects the nucleation and growth of acicular $\alpha$ phase.

The TEM microstructures are shown in Fig. 8. The diffraction spots indicate that the alloy consists of $\beta$ and $\alpha$ phases (Fig. 8(a)). At lower temperature (500 °C), finer acicular $\alpha$ phase is observed (Fig. 8(b)) because the larger subcooling at this temperature provides a larger nucleation driving force for the $\alpha$ phase. Moreover, low temperature limits the diffusion of alloying elements, thereby inhibiting the growth of the $\alpha$ phase [30−35]. The

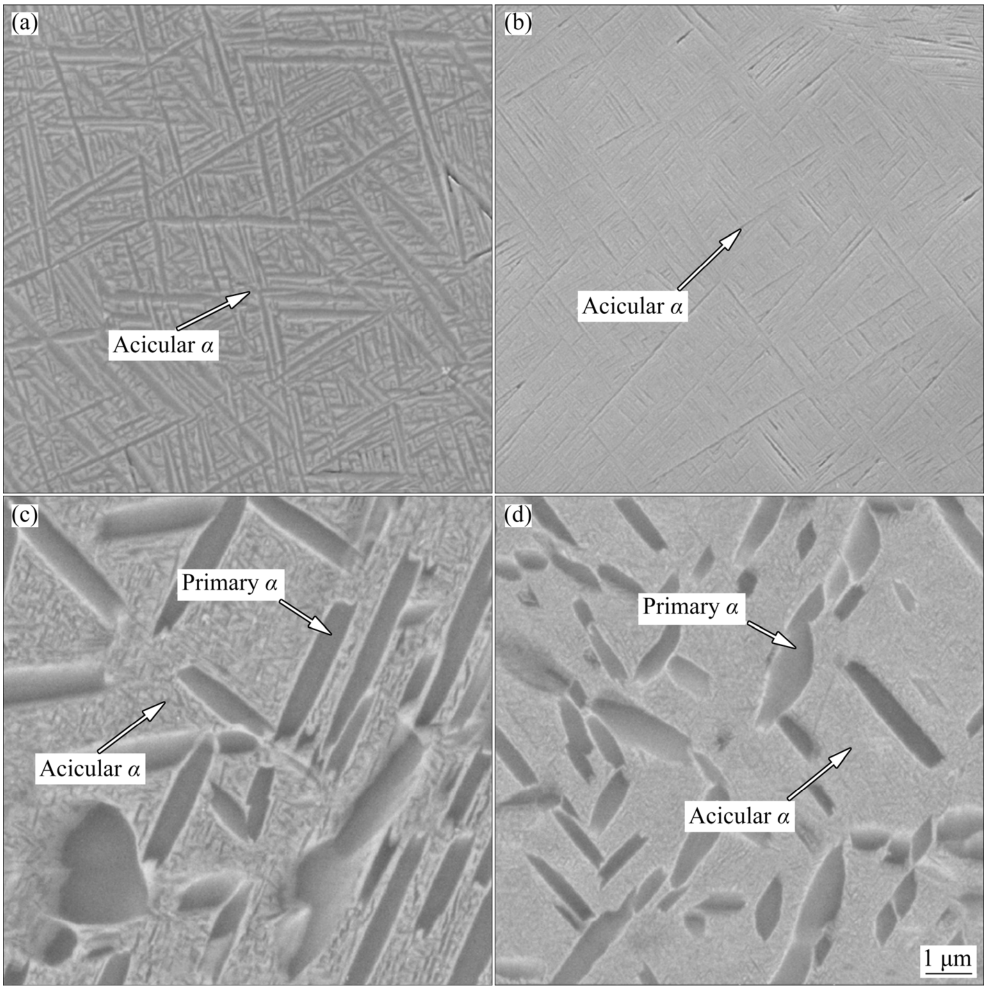

**Fig. 7** SEM microstructures of forged Ti-64-57 alloy: (a) 900 °C, 0.5 h + 600 °C, 6 h; (b) 900 °C, 0.5 h + 500 °C, 6 h; (c) 800 °C, 0.5 h + 600 °C, 6 h; (d) 800 °C, 0.5 h + 500 °C, 6 h

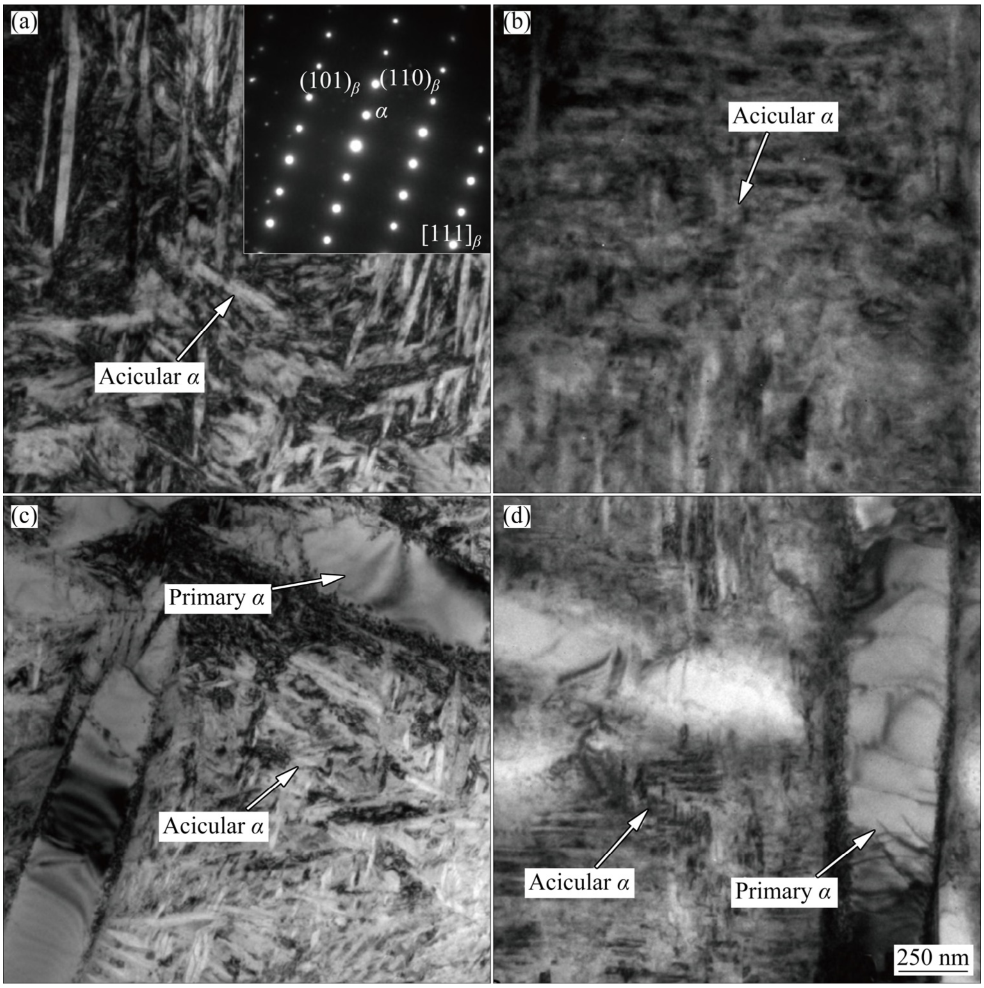

**Fig. 8** TEM microstructures of forged Ti-64-57 alloy: (a) 900 °C, 0.5 h + 600 °C, 6 h; (b) 900 °C, 0.5 h + 500 °C, 6 h; (c) 800 °C, 0.5 h + 600 °C, 6 h; (d) 800 °C, 0.5 h + 500 °C, 6 h

microstructure of the alloy after solution treatment in the $\alpha$+$\beta$ phase region and aging is composed of primary $\alpha$, acicular $\alpha$ and $\beta$ matrix (Figs. 8(c, d)). The number and size of primary $\alpha$ phase are determined by alloy composition, solution temperature, and forging [36].

The tensile properties of the alloy are shown in Fig. 9 and Table 2. As expected, the alloy exhibits high tensile strength (1409 and 1307 MPa) after solution treatment in a single-phase zone (900 °C). However, the elongation of the alloy is only ~1%. The alloy strengths after solution treatment in the two-phase region (800 °C) and aging state reach 1314 and 1227 MPa, respectively. However, the elongation of the alloy is greatly improved, reaching 12.5% and 10%, respectively.

### 3.5 Deformation and strengthening mechanism

Ti-64-57 alloy has obtained high strength (1314 MPa) and good plasticity (10.1%) after being solution-treated at 800 °C and aged at 500 °C. The high strength of the alloy is derived from the $\alpha/\beta$ phase boundary produced by a large number of secondary acicular $\alpha$, and the main contribution to good plasticity of the alloy is derived from the good deformability of the spherical primary $\alpha$ phase.

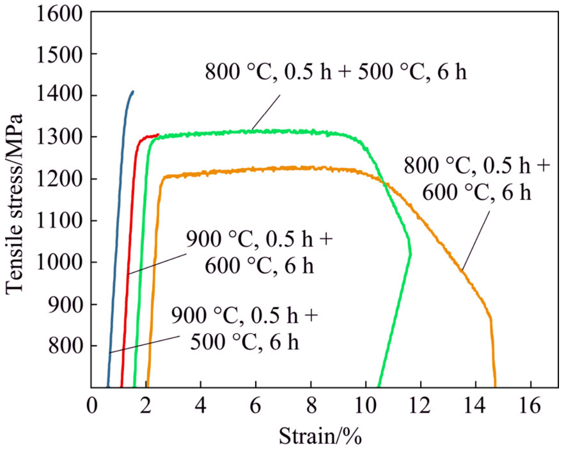

**Fig. 9** Stress−strain curves of forged Ti-64-57 alloy

**Table 2** Tensile properties of forged Ti-64-57 alloy

| Solution treatment | Aging treatment | Tensile strength/ MPa | Yield strength/ MPa | Elongation/ % |
|---|---|---|---|---|
| 800°C, 0.5 h, AC | 500 °C, 6 h, AC | 1314 | 1289 | 10.1 |
| | 600 °C, 6 h, AC | 1227 | 1198 | 12.5 |
| 900 °C, 0.5 h, AC | 500 °C, 6 h, AC | 1409 | 1399 | 0.7 |
| | 600 °C, 6 h, AC | 1307 | 1301 | 1.2 |

Thus, a detailed characterization of the primary *α* and the *α*/*β* interface of the acicular *α* phase is necessary to understand the plasticity and strengthening mechanism of the alloy.

First, a large number of dislocations are found inside the primary *α* phase (Fig. 10(a)). Previous studies [37] have shown that dislocation slip in the *α* phase in titanium alloys basically occurs on the prismatic $\{10\bar{1}0\}$ plane or the basal {0001} plane, whereas the $\langle a+c\rangle$ slip system can be partially activated only under the stress of the [0001] direction [38]. The high dislocation density may be related to the higher Al content in the primary *α* phase. In previous research [39], the increase of Al content in the *α* phase can effectively reduce the stacking fault energy of the alloy. Low stacking-fault energy indicates that dislocations can slip over a wide range, which is also the case in austenitic stainless steels with low stacking faults [40]. At the interface of the primary *α* phase, a black dislocation entanglement zone can be seen (Fig. 10(b)), indicating a large dislocation density at the interface of the *α* phase and the *β* matrix. The dislocations are gathered at the interface because such dislocations are hindered from slipping to the interface during the deformation, forming dislocation entanglements.

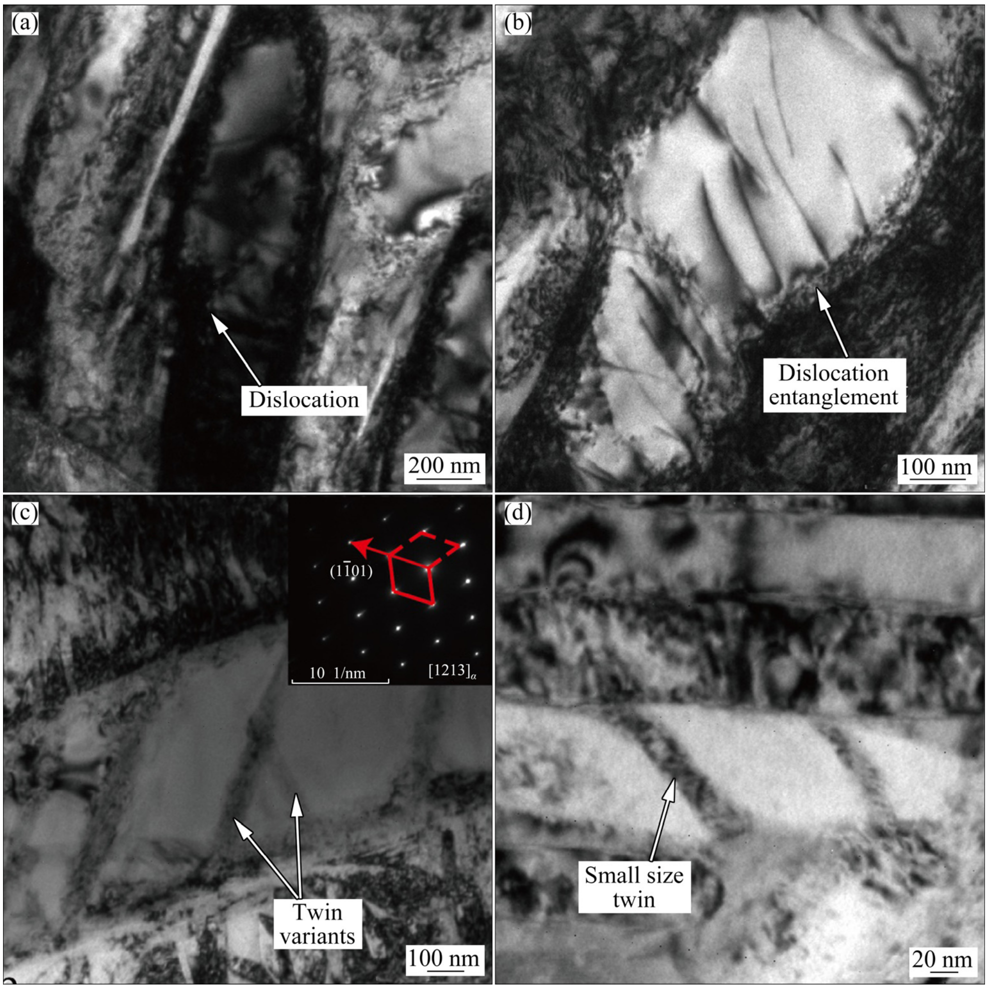

**Fig. 10** TEM images of primary *α* phase of Ti-64-57 alloy (800 °C, 0.5 h + 500 °C, 6 h): (a) Dislocation in primary *α* phase; (b) Dislocation entangled at boundary of primary *α*; (c) Twin variants in primary *α* phase (selected-area electron diffraction along $[1\bar{2}1\bar{3}]$ direction is used to identify $(1\bar{1}01)$ twins); (d) Small-sized twin in primary *α* phase

The research of QIN et al [41] showed that dislocation entanglement at the interface can cause stress concentration, resulting in the formation of micropores. When the micropore reaches a critical dimension, the micropore expands at a great rate and cracks are produced.

In other areas of the alloy, deformed twins in the primary $\alpha$ phase (Figs. 10(c, d)) are found. Notably, the twins have two variants: large variant and small variant. In the large variant, the length of the twins going through the entire $\alpha$ grain is approximately 1 μm and the width is 0.1 μm; whereas in the small variant, the length is approximately 0.5 μm (Fig. 10(c)). Results of the selected-area electron diffraction indicate that the variant belongs to the $(1\bar{1}01)[1\bar{1}0\bar{2}]$ twin crystal variant. In some primary $\alpha$, small-sized twins approximately 0.1 μm long and 0.02 μm thick are observed (Fig. 10(d)). CHEN et al [13] found twin variants of $(1\bar{1}01)[1\bar{1}0\bar{2}]$ system in the primary $\alpha$ phase in Ti-55511 alloy and showed that twin deformation is important in the adaptation of titanium alloy to severe deformation. The two different sizes of twins observed in Figs. 10(c, d) indicate the effect of the grain size of the $\alpha$ phase on the twin width, which means that a larger strain can be produced in the large $\alpha$ phase. Moreover, such twin sizes explain the poor deformability of the secondary $\alpha$ phase, although the twin system and the slip system in the secondary $\alpha$ phase are similar to those in the primary $\alpha$ phase. However, the size of the secondary $\alpha$ phase determines the size and volume fraction of the twin, which completely prevents this phase from assisting in the alloy deformation [42−44]. In summary, dislocation slip and twinning are the main deformation mechanisms of the primary $\alpha$ phase, in which a larger $\alpha$ phase can produce greater deformation.

After the alloy is solution-treated at 800 °C and aged at 500 °C, the interface structure of the secondary acicular $\alpha$ and $\beta$ phases is observed (Fig. 11). The $\alpha/\beta$ phase interface structure and the model diagram (board face) observed along the $[110]_\beta//[0001]_\alpha$ direction are shown in Figs. 11(a, b). The $\alpha/\beta$ interface strictly follows the Burgers vector relationship $[1\bar{1}\bar{1}]_\beta//[11\bar{2}0]_\alpha$. The interface consists of a traditional platform−step structure. The platforms are coherent, while the steps are incoherent. The length of the platform is not uniform, with an average of approximately 1.3 nm and the step height is always two-plane spacing $(1\bar{1}2)_\beta$, approximately 0.35 nm. The step is formed due to the mismatch with the atomic spacing along the $[1\bar{1}\bar{1}]_\beta$ and $[11\bar{2}0]_\alpha$ directions. Based on the model of ZHENG et al [45], the atomic spacing is 0.2875 nm in the $\beta$ phase and 0.2950 nm in the $\alpha$ phase, with a mismatch of approximately 2.6%. The internal stress generated by the atomic spacing mismatch can be alleviated by the platform−step structure. The angle of the habit plane of $\alpha$ and $\beta$ phases is approximately 15.3° with the coherent platform, which differs from a previous result of 12.9°. These findings may possibly be related to the difference in alloying elements.

The interface structure of $(\bar{1}11)_\beta/(\bar{1}\bar{1}20)_\alpha$ (cross-face) perpendicular to the $(110)_\beta/(0001)_\alpha$ face in Fig. 11(a) is shown in Figs. 11(c, d). The difference is that the $(\bar{1}11)_\beta/(\bar{1}\bar{1}20)_\alpha$ interface consists of a flat interface with no steps. Such difference is due to the small lattice mismatch along the [001] and [0001] directions. The mismatch degree reported is 1.2% [46], which is less than that previously mentioned. The smaller mismatch results in a relatively flat interface, and the stress caused by the mismatch of the lattice is eliminated by introducing a dislocation with a Burgers vector of $1/2[\bar{1}\bar{1}\bar{1}]_\beta$. At the $\alpha$ phase side of the interface (in the elliptical range in Fig. 11(c)), the arrangement of the atoms and the spacing of the atoms along the $[0001]_\alpha$ direction are not uniform, indicating stress concentration inside the $\alpha$ phase. WEN et al [47] observed high dislocation density inside the secondary $\alpha$ phase, which also proves the existence of internal stress. The platform−step structure at the $\alpha/\beta$ interface and lattice distortion effectively hinder the slip of dislocations and increase the difficulty of deformation, increasing the strength of the alloy.

### 3.6 Fracture mechanism

In order to further study the fracture mechanism, fracture analysis was carried out on the 800 °C solution-treated + 500 °C aged sample. The fracture surface perpendicular to the stretching direction is shown in Fig. 12. The macroscopic fracture surface is divided into the dimple zone and shear zone (Fig. 12(a)). In the shear zone, there is a smooth surface (Fig. 12(c)), and in the dimple zone there are large-sized dimples (Fig. 12(d)), which are characteristics of ductile fracture.

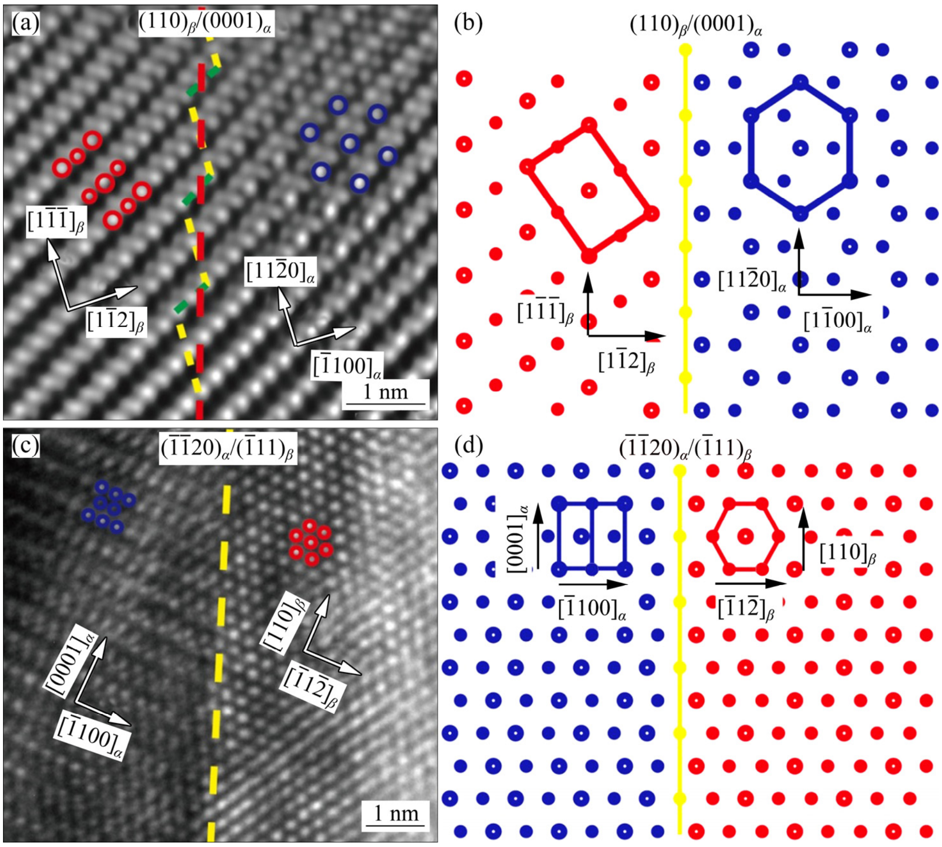

**Fig. 11** Acicular $\alpha$ and $\beta$ interfaces (800 °C, 0.5 h + 500 °C, 6 h): (a) HRTEM image of $(0001)_\alpha/(110)_\beta$ face (yellow dotted line is coherent interface, green dotted line is disconnected interface, and red dotted line is habitary plane); (b) $(0001)_\alpha/(110)_\beta$ plane atom model; (c) HRTEM image of $(\bar{1}\bar{1}20)_\alpha/(\bar{1}11)_\beta$ plane (yellow dotted line is interface); (d) $(\bar{1}\bar{1}20)_\alpha/(\bar{1}11)_\beta$ plane atom model

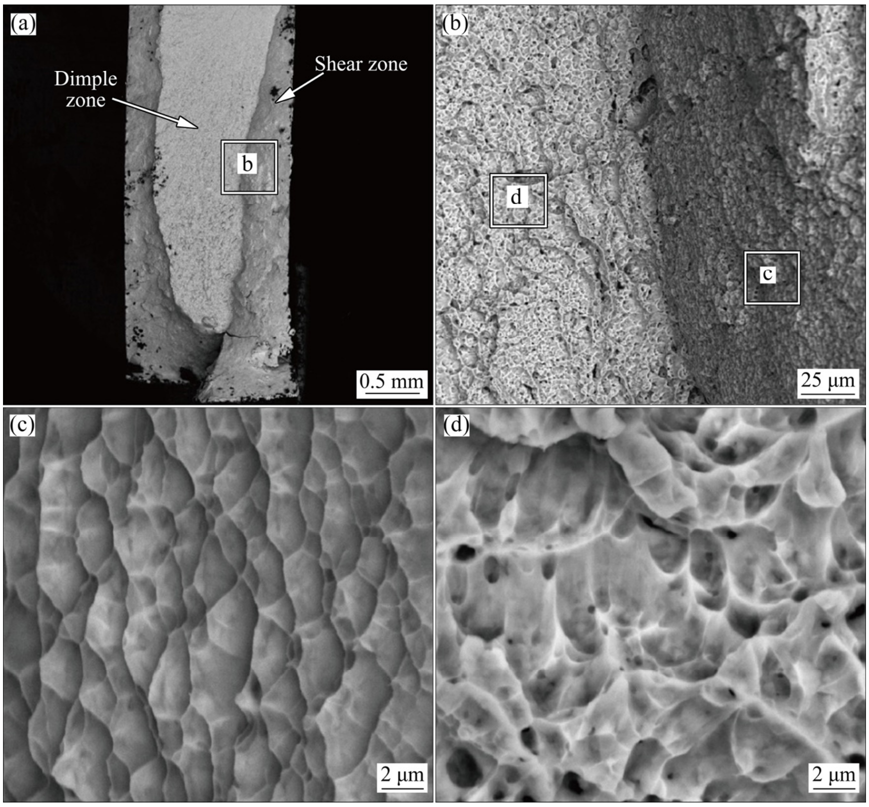

**Fig. 12** Fracture morphologies perpendicular to stretching direction: (a) Macroscopic fracture surface; (b) Shear zone and dimple zone; (c) Smooth surface; (d) Large dimples

The lateral section surface near the fracture surface is shown in Fig. 13. The tortuous fracture surface and narrowed cross-section in the macroscopic image indicate that significant necking occurs during the stretching process (Fig. 13(a)), which is the characteristic of ductile fracture. The nucleation position of the micro-voids can be seen near the fracture section. At Positions 1, 2 and 3 in Fig. 13(b), the micro-voids are all located near the interface between the primary $\alpha$ phase and $\beta$ transition structure. This is caused by the uneven strain derived from the difference in the strength of the primary $\alpha$ phase and the $\beta$ transition structure. The micro-void at Position 4 is located in the coarse $\beta$ transition microstructure. In Fig. 13(c), the primary $\alpha$ phase is torn, which is caused by the micro-voids located on the side of the primary $\alpha$ phase. In Fig. 13(d), the crack propagates along the primary $\alpha$ and $\beta$ interface, which is caused by the micro-void at the end of the primary $\alpha$ phase. Fracture analysis shows that the alloy is mainly characterized by ductile fracture. The nucleation position of the micro-voids is mainly at the interface of the primary $\alpha$ phase and $\beta$ transformation microstructure. The reason for the formation of micro-voids is the uneven strain between the primary $\alpha$ phase and $\beta$ transformation microstructure.

### 3.7 Comparison with other titanium alloys

In this work, a high-strength alloy is designed using the diffusion-multiple method. Through this method, Ti-64-57 alloy with the best performance is obatained. Figure 14 compares the performances of Ti-64-57 alloy with those of several commercial titanium alloys [48−59]. First, the yield strength of Ti-64-57 alloy greatly exceeds that of Ti-64 base alloy. Second, the strength and elongation of the alloy also reaches or exceeds those of Ti-5553, Ti-55511, and Ti-1023 alloys. Third, compared with alloys such as Ti-5553, Ti-55511 and Ti-1023, Mo, V, and Zr isomorphic $\beta$-stabilizing elements but not

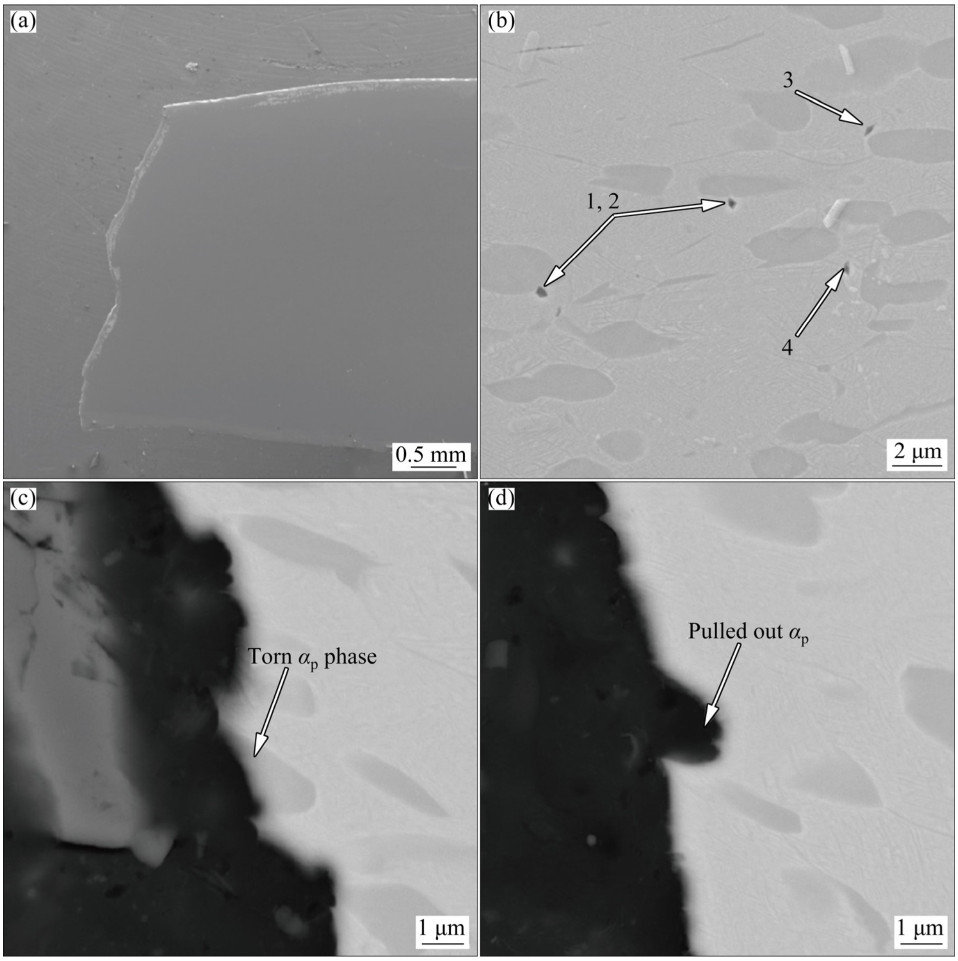

**Fig. 13** Lateral section surface morphologies near fracture surface: (a) Macroscopic lateral section surface; (b) Locations of micro-voids; (c) Primary $\alpha$ phase torn; (d) Primary $\alpha$ phase pulled out

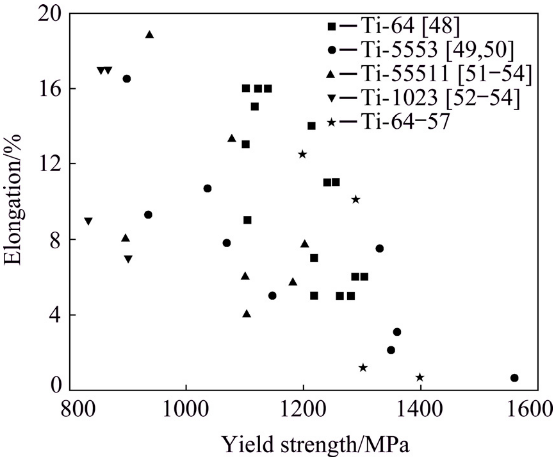

**Fig. 14** Comparison of tensile properties between Ti-64-57 alloy and several commercial titanium alloys

eutectoid elements such as Fe and Cr are used in Ti-64-75 alloy. Eutectoid elements are known to cause the segregation of alloying elements during smelting, and completely eliminating them during processing is difficult, such as the problem of Fe-rich $\beta$ spots in Ti-1023 alloy [60]. Therefore, Ti-64-57 alloy has advantage in melting and post processing stage.

## 4 Conclusions

(1) The Ti-64-57 alloy obtains the acicular $\alpha''$ phase after quenching, which may provide a heterogeneous nucleation sites for the $\alpha$ phase during aging. Hence, the alloy can obtain ultrafine $\alpha$ phase and high strength.

(2) The primary $\alpha$ phase produced by the solution treatment in the two-phase region can greatly increase the elongation of the alloy, and the deformation mechanism of the primary $\alpha$ phase is dislocation slip and twinning.

(3) Lattice distortion exists at the interface between the secondary $\alpha$ and $\beta$ phases. The broad interface of $(0001)_\alpha/(110)_\beta$ consists of a conventional platform−step structure. The angle between the platform and the habitual surface is 15.3°, whereas the cross-face of $(\bar{1}11)_\beta/(\bar{1}\bar{1}20)_\alpha$ is a flat interface with no steps.

## References

[1] THOMPSON S A. An overview of nickel−titanium alloys used in dentistry [J]. International Endodontic Journal, 2000, 33: 297−310.

[2] BOYER R R. An overview on the use of titanium in the aerospace industry [J]. Materials Science and Engineering A, 1996, 213: 103−114.

[3] JONES N G, DASHWOOD R J, JACKSON M, DYE D. $\beta$ phase decomposition in Ti−5Al−5Mo−5V−3Cr [J]. Acta Materialia, 2009, 57: 3830−3839.

[4] SCHWAB H, PALM F, KÜHN U, ECKERT J. Microstructure and mechanical properties of the near-beta titanium alloy Ti-5553 processed by selective laser melting [J]. Materials & Design, 2016, 105: 75−80.

[5] LAI M J, LI T, RAABE D. $\omega$ phase acts as a switch between dislocation channeling and joint twinning- and transformation-induced plasticity in a metastable $\beta$ titanium alloy [J]. Acta Materialia, 2018, 151: 67−77.

[6] MONZEN R, KAWAI R, OYAMA T, WATANABE C. Tensile-stress-induced growth of ellipsoidal $\omega$-precipitates in a Ti−20wt%Mo alloy [J]. Journal of Materials Science, 2016, 51: 2490−2498.

[7] BOYNE A, WANG D, SHI R P, ZHENG Y, BEHERA A, NAG S. Pseudospinodal mechanism for fine $\alpha/\beta$ microstructures in $\beta$-Ti alloys [J]. Acta Materialia, 2014, 64: 188−197.

[8] NI Y, RAO W, KHACHATURYAN A G. Pseudospinodal mode of decomposition in films and formation of chessboard-like nanostructure [J]. Nano Letters, 2009, 9: 3275−3281.

[9] NAG S, BANERJEE R, SRINIVASAN R, HWANG J Y, HARPER M, FRASER H L. $\omega$-assisted nucleation and growth of $\alpha$ precipitates in the Ti−5Al−5Mo−5V−3Cr−0.5Fe $\beta$ titanium alloy [J]. Acta Materialia, 2009, 57: 2136−2147.

[10] JIANG X J, JING R, MA M Z, LIU R P. The orthorhombic $\alpha''$ martensite transformation during water quenching and its influence on mechanical properties of Ti−41Zr−7.3Al alloy [J]. Intermetallics, 2014, 52: 32−35.

[11] MANTANI Y, TAJIMA M. Phase transformation of quenched $\alpha''$ martensite by aging in Ti−Nb alloys [J]. Materials Science and Engineering A, 2006, 438−440: 315−319.

[12] HAGHIGHI S E, LU H B, JIAN G Y, CAO G H, HABIBI D, ZHANG L C. Effect of $\alpha''$ martensite on the microstructure and mechanical properties of beta-type Ti−Fe−Ta alloys [J]. Materials & Design, 2015, 76: 47−54.

[13] CHEN W, LI C, ZHANG X, CHEN C, LIN Y C, ZHOU K. Deformation-induced variations in microstructure evolution and mechanical properties of bi-modal Ti-55511 titanium alloy [J]. Journal of Alloys and Compounds, 2019, 783: 709−717.

[14] GUO S, SHANG Y, ZHANG J S, MENG Q K, CHENG X N, ZHAO X Q. In situ synchrotron X-ray diffraction study of deformation behaviour of a metastable $\beta$-type Ti−33Nb−4Sn alloy [J]. Materials Science and Engineering A, 2017, 692: 81−89.

[15] KNOWLES K M, SMITH D A. The crystallography of the martensitic transformation in equiatomic nickel−titanium [J]. Acta Metallurgica, 1981, 29: 101−110.

[16] MARSHAL A, PRADEEP K G, MUSIC D, ZAEFFERER S, DE P S, SCHNEIDER J M. Combinatorial synthesis of high entropy alloys: Introduction of a novel, single phase,

body-centered-cubic FeMnCoCrAl solid solution [J]. Journal of Alloys and Compounds, 2017, 691: 683−689.

[17] ZHANG X D, LIU L B, ZHAO J C, WANG J L, ZHENG F, JIN Z P. High-efficiency combinatorial approach as an effective tool for accelerating metallic biomaterials research and discovery [J]. Materials Science and Engineering C, 2014, 39: 273−280.

[18] COURY F G, WILSON P, CLARKE K D, KAUFMAN M J, CLARKE A J. High-throughput solid solution strengthening characterization in high entropy alloys [J]. Acta Materialia, 2019, 167: 1−11.

[19] ZHAO J C, ZHENG X, CAHILL D G. High-throughput measurements of materials properties [J]. JOM, 2011, 63: 40−44.

[20] ZHAO J C, ZHENG X, CAHILL D G. High-throughput diffusion multiples [J]. Materials Today, 2005, 8: 28−37.

[21] BAI W M, XU G L, TAN M Y, YANG Z J, ZENG L J, WU D. Diffusivities and atomic mobilities in bcc Ti−Mo−Zr alloys [J]. Materials, 2018, 11: 1909−1925.

[22] WU D, ZHANG L G, LIU L B, BAI W M, ZENG L J. Effect of Fe content on microstructures and properties of Ti6Al4V alloy with combinatorial approach [J]. Transactions of Nonferrous Metals Society of China, 2018, 28: 1714−1723.

[23] WANG C Y, LI N, CUI Y W, PÉREZ-PRADO M T. Effect of solutes on the rate sensitivity in Ti−$x$Al−$y$Mo−$z$V and Ti−$x$Al−$y$Mo−$z$Cr $\beta$-Ti alloys [J]. Scripta Materialia, 2018, 149: 129−133.

[24] WANG C Y, YANG L W, CUI Y W, PÉREZ-PRADO M T. High throughput analysis of solute effects on the mechanical behavior and slip activity of beta titanium alloys [J]. Materials & Design, 2018, 137: 371−383.

[25] LEE S W, PARK C H, HONG J K, YEOM J T. Aging temperature dependence of $\alpha''$-martensite decomposition mechanism in Ti−Al−Fe−Si alloy [J]. Metallurgical and Materials Transactions A, 2018, 49: 5913−5918.

[26] BARRIOBERO-VILA P, REQUENA G, SCHWARZ S, WARCHOMICKA F, BUSLAPS T. Influence of phase transformation kinetics on the formation of $\alpha$ in a $\beta$-quenched Ti−5Al−5Mo−5V−3Cr−1Zr alloy [J]. Acta Materialia, 2015, 95: 90−101.

[27] ZHENG Y, WILLIAMS R, SOSA J, ALAM T, WANG Y, BANERJEE R. The indirect influence of the $\omega$ phase on the degree of refinement of distributions of the $\alpha$ phase in metastable $\beta$-titanium alloys [J]. Acta Materialia, 2016, 103: 165−173.

[28] XIAO W L, DARGUSCH M, KENT D, ZHAO X Q, MA C L. Activation of homogeneous precursors for formation of uniform and refined $\alpha$ precipitates in a high-strength $\beta$-Ti alloy [J]. Materialia, 2019, 9: 100557−100567.

[29] WU D, LIU L B, ZHANG L G, ZENG L J, SHI X. Investigation of the influence of Cr on the microstructure and properties of Ti6Al4V$x$Cr alloys with a combinatorial approach [J]. Journal of Materials Engineering and Performance, 2017, 26: 4364−4372.

[30] LONARDELLI I, GEY N, WENK H R, HUMBERT M, VOGEL S C, LUTTEROTTI L. In situ observation of texture evolution during $\alpha\rightarrow\beta$ and $\beta\rightarrow\alpha$ phase transformations in titanium alloys investigated by neutron diffraction [J]. Acta Materialia, 2007, 55: 5718−5727.

[31] AGUILAR C, PIO E, MEDINA A, PARRA C, MANGALARAJA R, MARTIN P. Effect of Sn on synthesis of nanocrystalline Ti-based alloy with fcc structure [J]. Transactions of Nonferrous Metals Society of China, 2020, 30: 2119−2131.

[32] WANG W, LI Z, SHEN W J, YIN F C, LIU Y. Phase equilibria of Zn−Al−Ti ternary system at 450 and 600 °C [J]. Transactions of Nonferrous Metals Society of China, 2020, 30: 1005−1016.

[33] HASHMI M L, WADOOD A. Microstructural, mechanical and shape memory characterizations of Ti−Mo−Sn alloys [J]. Transactions of Nonferrous Metals Society of China, 2020, 30: 688−700.

[34] GUO K K, LIU C S, CHEN S Y, DONG H H, WANG S Y. High pressure EIGA preparation and 3D printing capability of Ti−6Al−4V powder [J]. Transactions of Nonferrous Metals Society of China, 2020, 30: 147−159.

[35] XIA Y F, JIANG W, CHENG Q, JIANG L, JIN L. Hot deformation behavior of Ti−6Al−4V−0.1Ru alloy during isothermal compression [J]. Transactions of Nonferrous Metals Society of China, 2020, 30: 134−146.

[36] KAR S K, GHOSH A, FULZELE N, BHATTACHARJEE A. Quantitative microstructural characterization of a near beta Ti alloy, Ti-5553 under different processing conditions [J]. Materials Characterization, 2013, 81: 37−48.

[37] CASTANY P, PETTINARI-STURMEL F, CRESTOU J, DOUIN J, COUJOU A. Experimental study of dislocation mobility in a Ti−6Al−4V alloy [J]. Acta Materialia, 2007, 55: 6284−6291.

[38] DING R, GONG J, WILKINSON A J, JONES I P. $\langle c+a\rangle$ dislocations in deformed Ti−6Al−4V micro-cantilevers [J]. Acta Materialia, 2014, 76: 127−134.

[39] WANG W Y, ZHANG Y, LI J, ZOU C, TANG B, WANG H. Insight into solid-solution strengthened bulk and stacking faults properties in Ti alloys: A comprehensive first-principles study [J]. Journal of Materials Science, 2018, 53: 7493−7505.

[40] SALEH A A, PERELOMA E V, GAZDER A A. Microstructure and texture evolution in a twinning-induced-plasticity steel during uniaxial tension [J]. Acta Materialia, 2013, 61: 2671−2691.

[41] QIN D, LU Y, GUO D, ZHENG L, LIU Q, ZHOU L. Tensile deformation and fracture of Ti−5Al−5V−5Mo−3Cr−1.5Zr−0.5Fe alloy at room temperature [J]. Materials Science and Engineering A, 2013, 587: 100−109.

[42] YU Q, SHAN Z W, LI J, HUANG X, XIAO L, SUN J. Strong crystal size effect on deformation twinning [J]. Nature, 2010, 463: 335−338.

[43] XU S, TOTH L S, SCHUMAN C, LECOMTE J S, BARNETT M R. Dislocation mediated variant selection for secondary twinning in compression of pure titanium [J]. Acta Materialia, 2017, 124: 59−70.

[44] CHEN W, LV Y, ZHANG X, CHEN C, LIN Y C, ZHOU K C. Comparing the evolution and deformation mechanisms of lamellar and equiaxed microstructures in near $\beta$-Ti alloys during hot deformation [J]. Materials Science and Engineering A, 2019, 758: 71−78.

[45] ZHENG Y, WILLIAMS R E, VISWANATHAN G B, CLARK W A, FRASER H L. Determination of the structure

of $\alpha$-$\beta$ interfaces in metastable $\beta$-Ti alloys [J]. Acta Materialia, 2018, 150: 25−39.

[46] ZHENG Y, CLARK W A, FRASER H L. Characterization of the interfacial structure of coarse $\alpha$ precipitates in a metastable $\beta$-Ti alloy Ti−5Al−5Mo−5V−3Cr [J]. JOM, 2019, 71: 2291−2295.

[47] WEN M, LIU G, GU J F, GUAN W M, LU J. Dislocation evolution in titanium during surface severe plastic deformation [J]. Applied Surface Science, 2009, 255: 6097−6102.

[48] GUO P, ZHAO Y Q, ZENG W D, HONG Q. The effect of microstructure on the mechanical properties of TC4-DT titanium alloys [J]. Materials Science and Engineering A, 2013, 563: 106−111.

[49] IVASISHIN O M, MARKOVSKY P E, MATVIYCHUK Y U, SEMIATIN S L, WARD C H, FOX S. A comparative study of the mechanical properties of high-strength $\beta$-titanium alloys [J]. Journal of Alloys and Compounds, 2008, 457: 296−309.

[50] GHOSH A, SIVAPRASAD S, BHATTACHARJEE A, KAR S K. Microstructure–fracture toughness correlation in an aircraft structural component alloy Ti−5Al−5V−5Mo−3Cr [J]. Materials Science and Engineering A, 2013, 568: 61−67.

[51] NYAKANA S L, FANNING J C, BOYER R R. Quick reference guide for $\beta$ titanium alloys in the 00s [J]. Journal of Materials Engineering and Performance, 2005, 14: 799−811.

[52] SRINIVASU G, NATRAJ Y, BHATTACHARJEE A, NANDY T K, NAGESWARA R G. Tensile and fracture toughness of high strength $\beta$ titanium alloy, Ti−10V−2Fe−3Al, as a function of rolling and solution treatment temperatures [J]. Materials & Design, 2013, 47: 323−330.

[53] TERLINDE G T, DUERIG T W, WILLIAMS J C. Microstructure, tensile deformation, and fracture in aged Ti−10V−2Fe−3Al [J]. Metallurgical Transactions A, 1983, 14: 2101−2115.

[54] RAGHUNATHAN S L, DASHWOOD R J, JACKSON M, VOGEL S C, DYE D. The evolution of microtexture and macrotexture during subtransus forging of Ti−10V−2Fe−3Al [J]. Materials Science and Engineering A, 2008, 488: 8−15.

[55] MORAKABATI M, HAJARI A. Hot working behavior of near alpha titanium alloy analyzed by mechanical testing and processing map [J]. Transactions of Nonferrous Metals Society of China, 2020, 30: 1560−1573.

[56] YANG X, WANG W L, MA W J, WANG Y, YANG J G, LIU S F. Corrosion and wear properties of micro-arc oxidation treated Ti6Al4V alloy prepared by selective electron beam melting [J]. Transactions of Nonferrous Metals Society of China, 2020, 30: 2132−2142.

[57] LIU Z Q, MA R X, XU G J, WANG W B, SU Y H. Effects of annealing on microstructure and mechanical properties of $\gamma$-TiAl alloy fabricated via laser melting deposition [J]. Transactions of Nonferrous Metals Society of China, 2020, 30: 917−927.

[58] LI L, LI X Q, HU K, HE B L, MAN H. Brazeability evaluation of Ti−Zr−Cu−Ni−Co−Mo filler for vacuum brazing TiAl-based alloy [J]. Transactions of Nonferrous Metals Society of China, 2019, 29: 754−763.

[59] LI K, YANG P. Strain-induced $\alpha$-to-$\beta$ phase transformation during hot compression in Ti−5Al−5Mo−5V−1Cr−1Fe alloy [J]. Transactions of Nonferrous Metals Society of China, 2019, 29: 296−304.

[60] SAVVAKIN D G, CARMAN A, IVASISHIN O M, MATVIYCHUK M V, GAZDER A A, PERELOMA E V. Effect of iron content on sintering behavior of Ti−V−Fe−Al near-$\beta$ titanium alloy [J]. Metallurgical and Materials Transactions A, 2012, 43: 716−723.

# $\alpha''$相辅助形核获取超细 $\alpha$ 相高强度近 $\beta$ 态钛合金

王振宇[1,2]，刘立斌[1,2]，吴 迪[1,2,3]，章立钢[2]，王万林[3]，周科朝[1]

1. 中南大学 粉末冶金国家重点实验室，长沙 410083；
2. 中南大学 材料科学与工程学院，长沙 410083；
3. 中南大学 冶金与环境学院，长沙 410083

**摘　要**：采用多元扩散偶实验方法，设计具有超细 $\alpha$ 相的 Ti−6Al−4V−$x$Mo−$y$Zr ($0.5<x<12$, $0.5<y<14$，质量分数，%)合金。结果显示，Ti−6Al−4V−5Mo−7Zr 合金利用 $\alpha''$相为异质形核点，可获得超细 $\alpha$ 相，通过调整热处理工艺使多态组织合金获得强度和塑性的良好匹配。双态组织中初生 $\alpha$ 相的变形机制为位错滑移和 $\{1\bar{1}01\}$ 孪晶。合金的强化机制为次生 $\alpha/\beta$ 界面强化。$(0001)_\alpha/(110)_\beta$ 界面具有平台−台阶结构，$(\bar{1}\bar{1}20)_\alpha/(\bar{1}11)_\beta$ 界面为平直界面，没有台阶。

**关键词**：合金设计；高强钛合金；$\alpha''$相；$\alpha/\beta$ 界面；孪晶变形

**(Edited by Bing YANG)**